The Astrophysical Journal, 696:1084–1093, 2009 May 10 doi:10.1088/0004-637X/696/2/1084
© 2009. The American Astronomical Society. All rights reserved. Printed in the U.S.A.

FERMI LARGE AREA TELESCOPE OBSERVATIONS OF THE VELA PULSAR

A. A. Abdo[1,62], M. Ackermann[2], W. B. Atwood[3], R. Bagagli[4], L. Baldini[4], J. Ballet[5], D. L. Band[6,7], G. Barbiellini[8,9], M. G. Baring[10], J. Bartelt[2], D. Bastieri[11,12], B. M. Baughman[13], K. Bechtol[2], F. Bellardi[4], R. Bellazzini[4], B. Berenji[2], D. Bisello[11,12], R. D. Blandford[2], E. D. Bloom[2], J. R. Bogart[2], E. Bonamente[14,15], A. W. Borgland[2], A. Bouvier[2], J. Bregeon[4], A. Brez[4], M. Brigida[16,17], P. Bruel[18], T. H. Burnett[19], G. A. Caliandro[16,17], R. A. Cameron[2], F. Camilo[20], P. A. Caraveo[21], J. M. Casandjian[5], M. Ceccanti[4], C. Cecchi[14,15], E. Charles[2], A. Chekhtman[1,22], C. C. Cheung[7], J. Chiang[2], S. Ciprini[14,15], R. Claus[2], I. Cognard[23], J. Cohen-Tanugi[24], L. R. Cominsky[25], J. Conrad[26,27], R. Corbet[7], L. Corucci[4], S. Cutini[28], D. S. Davis[7,29], M. DeKlotz[30], C. D. Dermer[1], A. de Angelis[31], F. de Palma[16,17], S. W. Digel[2], M. Dormody[3], E. do Couto e Silva[2], P. S. Drell[2], R. Dubois[2], D. Dumora[32,33], C. Espinoza[34], C. Farnier[24], C. Favuzzi[16,17], D. L. Flath[2], P. Fleury[18], W. B. Focke[2], M. Frailis[31], P. C. C. Friere[35], Y. Fukazawa[36], S. Funk[2], P. Fusco[16,17], F. Gargano[17], D. Gasparrini[28], N. Gehrels[7,37], S. Germani[14,15], R. Giannitrapani[31], B. Giebels[18], N. Giglietto[16,17], F. Giordano[16,17], T. Glanzman[2], G. Godfrey[2], E. V. Gotthelf[20], I. A. Grenier[5], M.-H. Grondin[32,33], J. E. Grove[1], L. Guillemot[32,33], S. Guiriec[24], G. Haller[2], A. K. Harding[7], P. A. Hart[2], R. C. Hartman[7], E. Hays[7], G. Hobbs[38], R. E. Hughes[13], G. Jóhannesson[2], A. S. Johnson[2], R. P. Johnson[3], T. J. Johnson[7,37], W. N. Johnson[1], S. Johnston[38], T. Kamae[2], G. Kanbach[39], V. M. Kaspi[40], H. Katagiri[36], J. Kataoka[41], A. Kavelaars[2], N. Kawai[42,41], H. Kelly[2], M. Kerr[19], B. Kiziltan[43], W. Klamra[26], J. Knödlseder[44], M. Kramer[34], F. Kuehn[13], M. Kuss[4], J. Lande[2], D. Landriu[5], L. Latronico[4], B. Lee[45], S.-H. Lee[2], M. Lemoine-Goumard[32,33], M. Livingstone[40], F. Longo[8,9], F. Loparco[16,17], B. Lott[32,33], M. N. Lovellette[1], P. Lubrano[14,15], A. G. Lyne[34], G. M. Madejski[2], A. Makeev[22,1], R. N. Manchester[38], B. Marangelli[16,17], M. Marelli[21], M. N. Mazziotta[17], J. E. McEnery[7], S. McGlynn[26], M. A. McLaughlin[46], N. Menon[4,30], C. Meurer[27], P. F. Michelson[2], T. Mineo[47], N. Mirizzi[16,17], W. Mitthumsiri[2], T. Mizuno[36], A. A. Moiseev[6], M. Mongelli[17], C. Monte[16,17], M. E. Monzani[2], E. Moretti[8,9], A. Morselli[48,49], I. V. Moskalenko[2], S. Murgia[2], T. Nakamori[41], P. L. Nolan[2], A. Noutsos[34], E. Nuss[24], T. Ohsugi[36], N. Omodei[4], E. Orlando[39], J. F. Ormes[50], M. Ozaki[51], A. Paccagnella[11,52], D. Paneque[2], J. H. Panetta[2], D. Parent[32,33], M. Pearce[26], M. Pepe[14,15], M. Perchiazzi[17], M. Pesce-Rollins[4], L. Pieri[11], M. Pinchera[4], F. Piron[24], T. A. Porter[3], S. Rainò[16,17], R. Rando[11,12], S. M. Ransom[53], E. Rapposelli[4], M. Razzano[4], A. Reimer[2], O. Reimer[2], T. Reposeur[32,33], L. C. Reyes[54], S. Ritz[7,37], L. S. Rochester[2], A. Y. Rodriguez[55], R. W. Romani[2], M. Roth[19], F. Ryde[26], A. Sacchetti[17], H. F.-W. Sadrozinski[3], N. Saggini[4], D. Sanchez[18], A. Sander[13], P. M. Saz Parkinson[3], K. N. Segal[7], A. Sellerholm[27], C. Sgrò[4], E. J. Siskind[56], D. A. Smith[32,33], P. D. Smith[13], G. Spandre[4], P. Spinelli[16,17], M. Stamatikos[7], J.-L. Starck[5], F. W. Stecker[7], T. E. Stephens[7], M. S. Strickman[1], A. W. Strong[39], D. J. Suson[57], H. Tajima[2], H. Takahashi[36], T. Takahashi[51], T. Tanaka[2], A. Tenze[4], J. B. Thayer[2], J. G. Thayer[2], G. Theureau[23], D. J. Thompson[7], S. E. Thorsett[3], L. Tibaldo[11,12], O. Tibolla[58], D. F. Torres[59,55], A. Tramacere[60,2], M. Turri[2], T. L. Usher[2], L. Vigiani[4], N. Vilchez[44], V. Vitale[48,49], A. P. Waite[2], P. Wang[2], K. Watters[2], P. Weltevrede[38], B. L. Winer[13], K. S. Wood[1], T. Ylinen[61,26], and M. Ziegler[3]

[1] Space Science Division, Naval Research Laboratory, Washington, DC 20375, USA
[2] W. W. Hansen Experimental Physics Laboratory, Kavli Institute for Particle Astrophysics and Cosmology, Department of Physics and Stanford Linear Accelerator Center, Stanford University, Stanford, CA 94305, USA;rwr@astro.stanford.edu
[3] Santa Cruz Institute for Particle Physics, Department of Physics and Department of Astronomy and Astrophysics, University of California at Santa Cruz, Santa Cruz, CA 95064, USA
[4] Istituto Nazionale di Fisica Nucleare, Sezione di Pisa, I-56127 Pisa, Italy; massimiliano.razzano@pi.infn.it
[5] Laboratoire AIM, CEA-IRFU/CNRS/Université Paris Diderot, Service d'Astrophysique, CEA Saclay, 91191 Gif sur Yvette, France
[6] Center for Research and Exploration in Space Science and Technology (CRESST), NASA Goddard Space Flight Center, Greenbelt, MD 20771, USA
[7] NASA Goddard Space Flight Center, Greenbelt, MD 20771, USA
[8] Istituto Nazionale di Fisica Nucleare, Sezione di Trieste, I-34127 Trieste, Italy
[9] Dipartimento di Fisica, Università di Trieste, I-34127 Trieste, Italy
[10] Rice University, Department of Physics and Astronomy, MS-108, P.O. Box 1892, Houston, TX 77251, USA
[11] Istituto Nazionale di Fisica Nucleare, Sezione di Padova, I-35131 Padova, Italy
[12] Dipartimento di Fisica "G. Galilei," Università di Padova, I-35131 Padova, Italy
[13] Department of Physics, Center for Cosmology and Astro-Particle Physics, The Ohio State University, Columbus, OH 43210, USA
[14] Istituto Nazionale di Fisica Nucleare, Sezione di Perugia, I-06123 Perugia, Italy
[15] Dipartimento di Fisica, Università degli Studi di Perugia, I-06123 Perugia, Italy
[16] Dipartimento di Fisica "M. Merlin" dell'Università e del Politecnico di Bari, I-70126 Bari, Italy
[17] Istituto Nazionale di Fisica Nucleare, Sezione di Bari, 70126 Bari, Italy
[18] Laboratoire Leprince-Ringuet, École polytechnique, CNRS/IN2P3, Palaiseau, France
[19] Department of Physics, University of Washington, Seattle, WA 98195-1560, USA
[20] Columbia Astrophysics Laboratory, Columbia University, New York, NY 10027, USA
[21] INAF-Istituto di Astrofisica Spaziale e Fisica Cosmica, I-20133 Milano, Italy
[22] George Mason University, Fairfax, VA 22030, USA
[23] Laboratoire de Physique et Chemie de l'Environnement, LPCE UMR 6115 CNRS, F-45071 Orléans Cedex 02, and Station de radioastronomie de Nançay, Observatoire de Paris, CNRS/INSU, F-18330 Nançay, France
[24] Laboratoire de Physique Théorique et Astroparticules, Université Montpellier 2, CNRS/IN2P3, Montpellier, France
[25] Department of Physics and Astronomy, Sonoma State University, Rohnert Park, CA 94928-3609, USA
[26] Department of Physics, Royal Institute of Technology (KTH), AlbaNova, SE-106 91 Stockholm, Sweden
[27] Department of Physics, Stockholm University, AlbaNova, SE-106 91 Stockholm, Sweden
[28] Agenzia Spaziale Italiana (ASI) Science Data Center, I-00044 Frascati, Rome, Italy

[29] Center for Space Sciences and Technology, University of Maryland, Baltimore County, Baltimore, MD 21250, USA
[30] Stellar Solutions Inc., 250 Cambridge Avenue, Suite 204, Palo Alto, CA 94306, USA
[31] Dipartimento di Fisica, Università di Udine and Istituto Nazionale di Fisica Nucleare, Sezione di Trieste, Gruppo Collegato di Udine, I-33100 Udine, Italy
[32] CNRS/IN2P3, Centre d'Études Nucléaires Bordeaux Gradignan, UMR 5797, Gradignan, 33175, France
[33] Université de Bordeaux, Centre d'Études Nucléaires Bordeaux Gradignan, UMR 5797, Gradignan, 33175, France
[34] Jodrell Bank Centre for Astrophysics, University of Manchester, Manchester M13 9PL, UK
[35] Arecibo Observatory, Arecibo 00612, Puerto Rico
[36] Department of Physical Science and Hiroshima Astrophysical Science Center, Hiroshima University, Higashi-Hiroshima 739-8526, Japan
[37] University of Maryland, College Park, MD 20742, USA
[38] Australia Telescope National Facility, CSIRO, P.O. Box 76, Epping NSW 1710, Australia
[39] Max-Planck-Institut für Extraterrestrische Physik, Giessenbachstraße, 85748 Garching, Germany
[40] Department of Physics, McGill University, Montreal, PQ, H3A 2T8, Canada
[41] Department of Physics, Tokyo Institute of Technology, Meguro City, Tokyo 152-8551, Japan
[42] Cosmic Radiation Laboratory, Institute of Physical and Chemical Research (RIKEN), Wako, Saitama 351-0198, Japan
[43] UCO/Lick Observatories, 1156 High Street, Santa Cruz, CA 95064, USA
[44] Centre d'Étude Spatiale des Rayonnements, CNRS/UPS, BP 44346, F-30128 Toulouse Cedex 4, France
[45] Orbital Network Engineering, 10670 North Tantau Avenue, Cupertino, CA 95014, USA
[46] Department of Physics, West Virginia University, Morgantown, WV 26506, USA
[47] IASF Palermo, 90146 Palermo, Italy
[48] Istituto Nazionale di Fisica Nucleare, Sezione di Roma "Tor Vergata," I-00133 Rome, Italy
[49] Dipartimento di Fisica, Università di Roma "Tor Vergata," I-00133 Rome, Italy
[50] Department of Physics and Astronomy, University of Denver, Denver, CO 80208, USA
[51] Institute of Space and Astronautical Science, JAXA, 3-1-1 Yoshinodai, Sagamihara, Kanagawa 229-8510, Japan
[52] Dipartimento di Ingegneria dell'Informazione, Università di Padova, I-35131 Padova, Italy
[53] National Radio Astronomy Observatory (NRAO), Charlottesville, VA 22903, USA
[54] Kavli Institute for Cosmological Physics, University of Chicago, Chicago, IL 60637, USA
[55] Institut de Ciencies de l'Espai (IEEC-CSIC), Campus UAB, 08193 Barcelona, Spain
[56] NYCB Real-Time Computing Inc., 18 Meudon Drive, Lattingtown, NY 11560-1025, USA
[57] Department of Chemistry and Physics, Purdue University Calumet, Hammond, IN 46323-2094, USA
[58] Landessternwarte, Universität Heidelberg, Königstuhl, D 69117 Heidelberg, Germany
[59] Institució Catalana de Recerca i Estudis Avançats (ICREA), Barcelona, Spain
[60] Consorzio Interuniversitario per la Fisica Spaziale (CIFS), I-10133 Torino, Italy
[61] School of Pure and Applied Natural Sciences, University of Kalmar, SE-391 82 Kalmar, Sweden
Received 2008 November 5; accepted 2009 February 9; published 2009 April 22

ABSTRACT

The Vela pulsar is the brightest persistent source in the GeV sky and thus is the traditional first target for new γ-ray observatories. We report here on initial *Fermi* Large Area Telescope observations during verification phase pointed exposure and early sky survey scanning. We have used the Vela signal to verify *Fermi* timing and angular resolution. The high-quality pulse profile, with some 32,400 pulsed photons at $E \geqslant 0.03$ GeV, shows new features, including pulse structure as fine as 0.3 ms and a distinct third peak, which shifts in phase with energy. We examine the high-energy behavior of the pulsed emission; initial spectra suggest a phase-averaged power-law index of $\Gamma = 1.51^{+0.05}_{-0.04}$ with an exponential cutoff at $E_c = 2.9 \pm 0.1$ GeV. Spectral fits with generalized cutoffs of the form $e^{-(E/E_c)^b}$ require $b \leqslant 1$, which is inconsistent with magnetic pair attenuation, and thus favor outer-magnetosphere emission models. Finally, we report on upper limits to any unpulsed component, as might be associated with a surrounding pulsar wind nebula.

Key words: gamma rays: observations – pulsars: individual (PSR B0833-45)

Online-only material: color figures

1. INTRODUCTION

Radio pulsations at $P = 89$ ms from PSR B0833-45 (=PSR J0835-4510) in the Vela supernova remnant were discovered by Large et al. (1968). This pulsar is bright ($S_{1.4}$ GHz ≈ 1.5 Jy), young (characteristic age $\tau_c = P/2\dot{P} = 11$ kyr), and energetic ($\dot{E}_{\rm SD} = 6.9 \times 10^{36} I_{45}$ erg s^{-1}, for a neutron star moment of inertia $10^{45} I_{45}$ g cm^2). It is embedded in a flat spectrum radio synchrotron nebula (see Frail et al. 1997) and is surrounded by a bright X-ray wind nebula displaying remarkable toroidal symmetry (Helfand et al. 2001; Pavlov et al. 2003). A VLBI parallax measurement provides a well-determined distance of $D = 287^{+19}_{-17}$ pc (Dodson et al. 2003), improving on earlier optical *Hubble Space Telescope* (*HST*) measurements (Caraveo et al. 2001). This proximity means that the spin-down energy flux at Earth, $\dot{E}_{\rm SD}/4\pi d^2$, is second only to that of the Crab pulsar and ensures that Vela is among the most intensely studied neutron stars, particularly at high energies.

Pulsed γ-ray emission from Vela was first detected during the *SAS 2* mission (Thompson et al. 1975); it is, in fact, the brightest persistent source of celestial γ-rays and has been the proving ground of GeV observatories ever since. The basic source properties discovered by *SAS 2* were elaborated using observations by *COS B* (Kanbach et al. 1980) and Compton Gamma Ray Observatory (*CGRO*)/EGRET (Kanbach et al. 1994): the source is ~100% pulsed with no convincing evidence for year-scale variations, the two γ-ray peaks are separated by 0.42 in pulsar phase and the first peak lags the radio peak by 0.12 in phase. The source spectrum is hard with an average photon index $\Gamma = 1.7$ with evidence of a cutoff above 2–4 GeV. The

[62] National Research Council Research Associate.

Table 1
Early LAT Observations of PSR B0833-45

Date	MJD	Primary Mode	$N(E > 0.03$ GeV)[a]	Notes
2008 Jun 30–Jul 4	54647.40–54651.36	Sky survey	1859	LAT First light
2008 Jul 4–Jul 15	54651.38–54662.10	Survey + pointings	5172	LAT Calibrations
2008 Jul 15–Jul 19	54662.12–54666.08	Pointings +survey + limb following	1170	Pointed Obs. Tuning
2008 Jul 19–Jul 22*[b]	54666.10–54669.14	Pointed Vela+ 2nd target	7751	Pointed Obs. Tuning
2008 Jul 22–Jul 24	54669.16–54671.41	Pointed Vela+ 2nd target	3212	Pointed Obs. Tuning
2008 Jul 24–Jul 30*	54671.36–54677.45	Pointed Vela+ 2nd target	7607	Pointed Obs. Tuning
2008 Jul 30–Aug 3	54677.45–54681.66	Polar study + sky survey tuning	886	Nominal Ops.
2008 Aug 3–Sep 14*	54687.68–54723.91	Sky survey	26680	Nominal Ops.[c]

Notes.
[a] All photons (pulsed and background) within 5° of PSR B0833-45, zenith angle $z < 105°$, event class *Pass6-Diffuse*.
[b] Observations marked by asterisk are those used for spectral studies.
[c] L&EO ended on August 11.

most detailed study, to date, of the γ-ray pulsations is that of Fierro et al. (1998), which produced a high signal-to-noise pulse profile and evidence for phase-resolved spectral variations. As the present work was being prepared for submission, the AGILE team reported their initial results on γ-ray pulsars, including Vela (Pellizzoni et al. 2009); the results, given the more limited count rates and energy resolution, are broadly consistent with our conclusions described below.

With the successful launch of the *Fermi Gamma-Ray Space Telescope*, formerly *GLAST*, observatory on 2008 June 11, we have a new opportunity to examine the high-energy behavior of the Vela pulsar and to study this archetype of the young, energetic pulsars in detail. During Launch and Early Operations (L&EO) phase, the *Fermi* mission targeted the Vela pulsar for a number of pointed observations, in addition to coverage during initial tests of the sky survey mode. In the latter mode, the instrument axis is offset north and south of the zenith during alternate orbits to provide near-uniform sky coverage every 3 hr. One main purpose of these early observations was to tune the Large Area Telescope (LAT) performance on celestial γ-ray sources. However, the initial results on Vela itself are of interest, including new high-energy features in the pulse profile, an improved measurement of the high-energy cutoff in the pulsar spectrum, and a search for associated pulsar wind nebula (PWN) emission at GeV energies.

2. RADIO TIMING OBSERVATIONS

The Vela pulsar is young and exhibits substantial timing irregularities. This means that the optimal use of the Vela γ-ray photons, which arrive at an orbit-averaged rate of one every 4 minutes during LAT sky survey observations, requires a simultaneous radio ephemeris. The radio ephemeris is obtained using observations made with the 64 m Parkes radio telescope as part of the overall program for pulsar monitoring in support of the *Fermi* mission (Smith et al. 2008). A total of 27 times of arrival (TOAs) were obtained at a frequency of 1.4 GHz over the period of the LAT observations. The median error in each TOA is 1.7 μs. Fits to the TOAs were made with the pulsar's rotational frequency and frequency derivative as free parameters, and the ephemeris created from these data maintains phase with a root-mean-square (rms) residual of 90 μs, or 10^{-3} of pulsar phase, throughout the LAT observations. No large timing irregularities or glitches were detected. An accurate determination of the pulsar's dispersion measure of $67.95 \pm 0.03\,\mathrm{cm}^{-3}$ pc was obtained by measuring the delay in the TOAs of the pulse across the 256 MHz bandpass of the 1.4 GHz receiver. This allows extrapolation of the radio ephemeris to infinite frequency with an error of ~60 μs. Photon arrival times were referred to the solar-system barycenter and pulse phases were assigned using the standard pulsar timing software TEMPO2 (Hobbs et al. 2006).

We thus can assign a pulsar phase to the γ-ray photons referenced to the radio with high confidence. Gamma-ray events recorded with the LAT have timestamps that derive from a GPS clock on the *Fermi* satellite. Prelaunch ground timing measurements using cosmic muons seen coincidentally in the LAT and in an independent counting system demonstrated that the LAT measures event times relative to the spacecraft clock with a resolution of better than 300 ns. On orbit, satellite telemetry indicates a comparable resolution. The contribution to the barycenter times from uncertainty in the LAT's position is negligible. It is also useful to confirm the absolute timing using celestial signals; as of this writing the six classical pulsars detected by EGRET have provided good quality LAT pulse profiles. The phasing of the radio and γ-ray peaks is consistent with the best EGRET results, ensuring absolute timing relative to the radio time system better than ~1 ms.

3. GAMMA-RAY OBSERVATIONS

The LAT instrument on *Fermi* is described by Atwood et al. (2009) and references therein. The LAT is an electron–positron pair production telescope featuring solid state silicon trackers sensitive to photons from <30 MeV to >300 GeV. It has a large ~2.4 sr field of view, and compared to earlier γ-ray missions, has a large effective area (~8000 cm^2 on axis), improved resolution (~0.5, 68% containment radius at 1 GeV for events collected in the 'front' section with thin radiator foils) and small dead time (~25 μs event^{-1}). We report here on the LAT's initial observations of the Vela pulsar, using data collected during 35 days of on-orbit verification tests and the initial ~40 days of the ongoing first-year sky survey. These data already suffice to illustrate the power of the LAT for astronomical observations and, indeed, show several new features in the radiation of this well-known γ-ray pulsar.

Table 1 contains a journal of the Vela coverage, along with numbers of photons with measured energy above 0.03 GeV recorded within a radius of 5° of the pulsar, including background photons. For both pointed and survey observations, we exclude events within 8° of the Earth's limb to minimize contamination by "Earth albedo" photons.

During the L&EO period, the instrument configuration was being tuned for optimum performance. Accordingly, the

Table 2
Phase-Averaged Spectral Points for the Vela Pulsar

Energy (GeV)	Differential Flux (F) (erg cm^{-2} s^{-1})	$\Delta F_{\rm stat}$	$\Delta F_{\rm syst}$	$\Delta F_{\rm tot}^{\rm a}$
0.14	1.381E-09	5.805E-11	2.952E-10	3.009E-10
0.18	1.385E-09	5.191E-11	1.601E-10	1.683E-10
0.22	1.514E-09	3.895E-11	2.261E-10	2.294E-10
0.28	1.734E-09	4.212E-11	2.301E-10	2.340E-10
0.35	1.953E-09	4.563E-11	2.232E-10	2.279E-10
0.45	2.129E-09	5.066E-11	2.625E-10	2.674E-10
0.56	2.088E-09	5.289E-11	1.671E-10	1.752E-10
0.71	2.200E-09	5.711E-11	2.755E-10	2.814E-10
0.89	2.405E-09	6.505E-11	3.006E-10	3.076E-10
1.12	2.417E-09	7.111E-11	2.185E-10	2.298E-10
1.41	2.493E-09	8.007E-11	4.626E-10	4.695E-10
1.78	2.312E-09	8.507E-11	4.101E-10	4.188E-10
2.24	2.273E-09	9.770E-11	4.164E-10	4.277E-10
2.82	2.005E-09	1.055E-10	3.896E-10	4.036E-10
3.55	1.617E-09	1.052E-10	4.524E-10	4.645E-10
4.47	1.357E-09	1.135E-10	4.286E-10	4.434E-10
5.62	1.019E-09	1.116E-10	1.854E-10	2.164E-10
7.08	4.403E-10	8.276E-11	1.931E-10	2.101E-10
8.91	4.435E-10	9.914E-11	1.870E-10	2.116E-10
11.22	9.390E-11	6.150E-11	0.000E+00	2.542E-11
14.13	4.191E-11	4.550E-11	0.000E+00	3.043E-11
17.78	1.169E-10	8.417E-11	1.053E-11	8.483E-11
22.39	0.000E+00	0.000E+00	0.000E+00	0.000E+00
28.18	0.000E +00	0.000E+00	0.000E+00	0.000E+00

Note. [a] $\Delta F_{\rm syst}$ is the systematic error on the flux and $\Delta F_{\rm syst}$ are the statistical errors on the flux, while $\Delta F_{\rm tot}$ is the total error on the flux.

knowledge of the energy scale and effective area are more limited than for routine operations. We discuss how these data verify the LAT photon selection, effective area, timing, photon energy measurement, and the variation of the point-spread function (PSF) with energy. These results may be of use to researchers seeking to predict *Fermi* capabilities during longer exposures of fainter sources, in both sky survey and pointed mode.

4. RESULTS

4.1. Pulse Profiles

After calibration of the LAT pointing axis on a large set of identified high latitude γ-ray sources, we find that the best-fit position of the Vela point source is within 0.′5 of the radio pulsar position with a statistical error of 0.′4 (95%); the LAT has unprecedented accuracy for localization of bright hard γ-ray sources, although some systematic uncertainties remain.

The Vela pulsar is embedded in the bright γ-ray emission of the Galactic plane, which is particularly strong at low energies. Further, the LAT, like all pair production telescopes, has an angular resolution dominated by scattering at low photon energies $\theta_{68} \approx 0.^{\circ}8 E_{\rm GeV}^{-0.75}$ (see below). Thus, selection of photons from an energy-dependent region of interest (ROI) around Vela is important; the best selection depends on the desired product. Here, we seek pulse profiles with good signal to noise over a broad energy range, so we select photons within an angle $\theta < {\rm Max}[1.6 - 3\,{\rm Log}_{10}(E_{\rm GeV}), 1.3]$ deg of the pulsar position. This includes a larger fraction of the PSF at high energies, where the background is relatively faint. We use "Diffuse" class events, those reconstructed events having the highest probability of being photons.

In this energy-dependent aperture, we have 32,400 ± 242 pulsed photons and 2780 ± 53 background photons with measured energy >0.03 GeV. Figure 1 shows the 0.1–10 GeV pulse profile from this ROI with the peak of the radio pulsar signal at phase 0. To highlight the fine structure, we plot in Figure 1 the pulse profile using variable-width bins, each containing 200 counts. These counts, divided by the bin width, give the photon flux in each phase interval; these phase bin

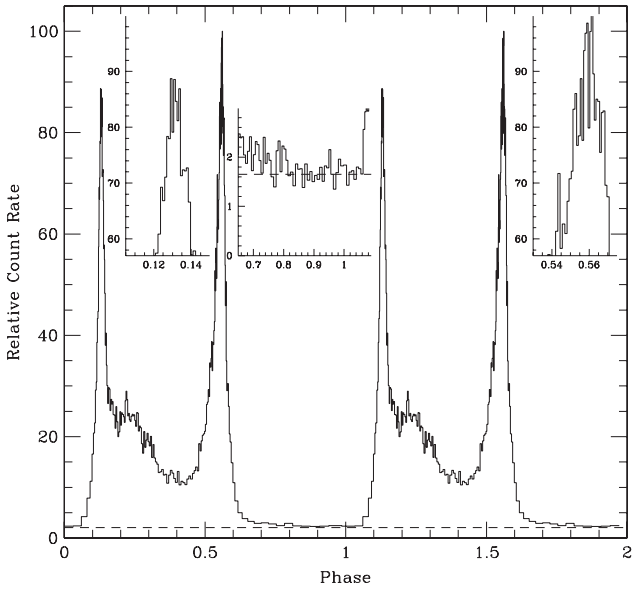

Figure 1. Vela broadband ($E = 0.1 - 10$ GeV) pulse profile for all photons from an energy-dependent ROI. Two pulse periods are shown. The peak of the radio pulse is at phase $\phi = 0$. The count rate is shown in variable-width phase bins with a constant number of counts. The dashed line shows the background level, as estimated from a surrounding annulus during the off-pulse phase. Insets show the pulse shape near the peaks and in the off-pulse region.

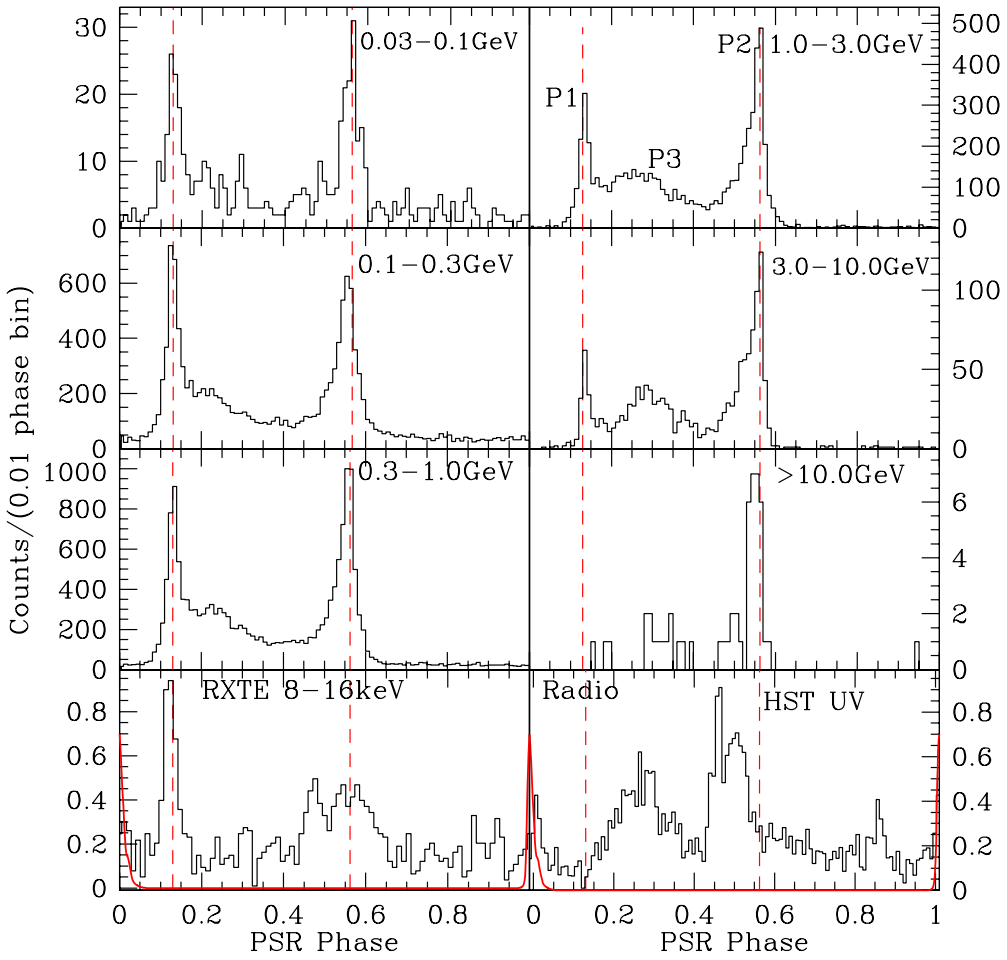

Figure 2. Evolution of the Vela γ-ray pulse profile over three decades of energy. Each pulse profile is binned to 0.01 of pulsar phase, and dashed lines show the phases of the P1 and P2 peaks determined from the broadband light curve. In the top right panel, we label the main peaks P1, P2, and P3. In the bottom panels, we show at left the 8–16 keV *RXTE* pulse profile of Harding et al. (2002) along with the radio pulse profile (in red). At lower right, the 4.1–6.5 eV *HST*/STIS NUV pulse profile of Romani et al. (2005) is shown for comparison.

(A color version of this figure is available in the online journal.)

fluxes thus have a 1σ Poisson statistical error of 7%. The pulse profile is normalized to 100 at the pulse peak. Three insets show structure near the first peak (P1), second peak (P2), and "off-pulse" window at a finer scale. These peaks are at pulsar phases $\phi = 0.130 \pm 0.001$ and 0.562 ± 0.002, respectively.

The peaks are asymmetric. In particular, P2 has a slow rise and a fast fall. P1 also has a steep outer edge with the fall somewhat slower. We fit each peak in Figure 1 with two half-Lorentzian functions (with different widths for the leading and trailing sides) over phase intervals which avoided the complex bridge flux ($0.11 < \phi < 0.16$ for P1, $0.53 < \phi < 0.59$ for P2). The outer edges of the two peaks had consistent Lorentzian half-widths of $\phi = 0.012 \pm 0.001$. Extra structure at the pulse peaks made the half maximum widths somewhat smaller ($\phi = 0.009 \pm 0.002$; 0.8 ms). The falling edge of peak 1 has a Lorentzian half-width of $\phi = 0.017 \pm 0.0015$, while the rising edge of P2 has a width $\phi = 0.027 \pm 0.005$. Both peaks show apparently significant structure on scales as small as $\delta\phi \approx 0.003$ ($\sim$300 μs), but additional counts are required to fully probe the pulse profile at this scale. We also show an inset of the "off-pulse region" ($\phi = 0.65$–1.05), with 50 counts bin^{-1} to show fine structure. Here and in the main panel, the dashed line shows the estimated residual unpulsed background counts in our energy-dependent ROI, as measured from the pulse minimum. This is in good agreement with a background level estimated from 3° to 5° around the pulsar. We see that, as for other nonradio Vela pulse profiles, there is a faint tail of pulsed emission in this region, reaching nondetectability only near $\phi = 0.8$–1.0. We estimate that this "off-pulse" window contains 235 ± 15 pulsed photons (7.3×10^{-3} of the pulsed flux).

There is dramatic energy evolution in the γ-ray pulse profile. Figure 2 shows pulse profiles from six energy bins, covering three decades of the LAT data, drawn from our energy-dependent aperture. Note that the relatively large aperture at low energies leads to larger off-pulse flux from the surrounding background. We should also caution that, with the present limited accuracy in energy measurement below 0.1 GeV, some higher energy photons may leak into the lowest energy bin. The most prominent pulse feature is a decrease of P1 relative to P2 with increasing energy; P1 is not detectable above $\sim$10 GeV (Figure 2). This confirms a trend seen in the EGRET data for the Crab, Vela, and Geminga pulsars—the second pulse dominates at the highest energies (Thompson 2001). Interestingly, at the lower energies, below $\sim$120 MeV, the trend is reversed with P1 weakening again with respect to P2. We do not find any statistically significant evidence for shifts in the phases of the narrow P1 and P2 pulse components with energy. These structures, spanning together <0.07 of the rotational phase, contain

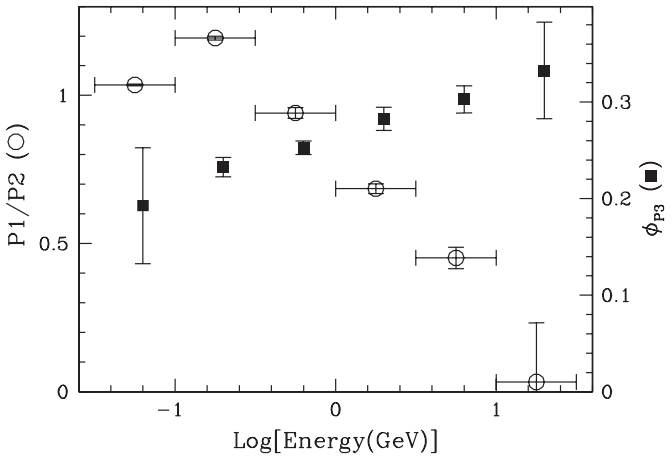

Figure 3. Evolution of the P1/P2 pulse peak ratio (open circles) and the P3 pulse peak phase (solid squares) with energy.

emission dominating over three decades of the pulsar photon output.

The "bridge" region between the peaks also shows appreciable structure with a trailing shoulder of P1 shifting to later phase. At >1 GeV, it is clear that this is a distinct pulse component (P3) with a peak at $\phi \sim 0.27$ in the 3–10 GeV band (Figure 2). Note that this peak shifts in phase by $\delta\phi \approx 0.14$ between 0.2 and 15 GeV (Figure 3).

To compare with the lower energy structure, we show at bottom left of Figure 2 the 8–16 keV nonthermal X-ray pulse measured by *RXTE* (Harding et al. 2002). On the right, we similarly show the 4.1–6.5 eV NUV *HST* STIS/MAMA pulse profile of Romani et al. (2005). The 1.4 GHz radio pulse profile, whose peak defines phase $\phi = 0$, runs across the bottom two panels. Both the optical/UV and the hard X-rays are dominated by nonthermal magnetospheric emission. In contrast, the <1 keV soft X-ray flux is dominated by thermal emission from the neutron star surface (e.g., Manzali et al. 2007), making it much more difficult to trace the nonthermal peaks through this intermediate energy band.

We may compare components in the UV and hard X-ray pulse profiles shown with those of the nonthermal γ-ray pulsations. In particular, we should note that the γ-ray P1 component is dominant in the non-thermal X-rays. This component is absent in the optical/UV, but pulse profiles at these energies have a strong peak in the bridge region at $\phi \sim 0.25$, well matched in phase to the P3 structure in the >GeV pulse profiles. This possible connection between optical pulses and the γ-ray bridge emission was already noted by Kanbach et al. (1980). Note that the profile for UV energies has a distinct sharp pulse coincident with the radio at $\phi = 0$. While the general slope of the faint $\phi = 0.65$–1.05 γ-ray emission matches that of the UV, no sharp γ-ray pulse components are yet visible in this phase interval.

4.2. The PSF and a Search for Unpulsed Emission

Figure 1 makes it clear that the Vela extraction region is strongly dominated by the pulsed emission. However, there are substantial phase windows where the pulsar is very faint. Figure 4 presents *Fermi* γ-ray images of the Vela pulsar in three energy bands in the LAT range separated into the on- ($\phi = 0.05$–0.65) and off- ($\phi = 0.65$–1.05) pulse phase regions. The images (except for the low count high-energy off-pulse frame) are smoothed by Gaussians (with FWHM= 1.°2, 0.°7, and 0.°2 for the low- to high-energy images, respectively). The off-pulse images show the bright diagonal band of the Galactic diffuse emission, with appreciable structure. Comparison with the PSF contours (red) shows that this is resolved in the vicinity of Vela at the higher energies. While a clump of extended emission surrounds the pulsar position on the few degree scale, it is at present not possible to associate this flux with known Vela PWN structures (e.g., the Vela X TeV PWN, contours in the middle energy band).

We have subtracted these off-pulse images (scaled by 1.5× to normalize exposure) from the on-pulse images and plotted (error bars) the profile of the resulting point source (bottom panels). The lines show simulations of the expected PSF from prelaunch calibrations ("Pass6"), computed for a source with a Vela-like spectrum and off-axis angles similar to the actual observations. The agreement is quite good. As a first attempt at constraining unpulsed (e.g., PWN) emission from Vela, we have attempted to fit for a point source in the off-pulse phase window, fixed at the position of the pulsar. Using 0.1–10 GeV photons in an 8° ROI in the $\phi = 0.65$–1.05 phase interval, we derive a 95% CL upper limit on the flux of $1.8 \times 10^{-7} \gamma$ cm^{-2} s^{-1}. After subtracting the estimated remnant pulsed flux in this window (0.73% of the phase-averaged flux) and scaling to the full pulse phase, this provides a limit on an unpulsed point source at the position of Vela of 2.8% of the $E > 100$ MeV pulsed emission count rate. More photons, especially at higher energy, will be required to search for a resolved PWN correlated with the TeV or radio structures.

4.3. Energy Spectrum

To study the phase-averaged spectrum of Vela, we used the standard maximum-likelihood spectral estimator "gtlike" to be provided with the *Fermi* SSC science tools. This fits a source model to the data, along with models for the isotropic (instrumental and extragalactic) and structured Galactic backgrounds. The instrumental background was comparable to estimates from prelaunch simulation (Atwood et al. 2009). We used data from the observation spans indicated in Table 1, selecting photons with $E > 0.1$ GeV within 15° of Vela. Our basic model for the spectrum of Vela is a simple power law with an exponential cutoff.

With the large number of events collected for Vela, the statistical errors are very small. Systematic errors for the LAT are still under investigation (A. A. Abdo et al. 2009, in preparation). Here, we adopt conservative estimates of the systematic uncertainty in the LAT effective area, derived from the on-orbit estimation of the photon selection efficiency as function of energy and off-axis angle. This estimation has been made by comparing Vela on-pulse event selection to event selection in the off-phase bins. This allows an estimate of the efficiency for a pure photon sample, which is compared with our current simulation of the LAT response. We conducted this exercise for a range of energy and off-axis angle bins, and use the precision of the resulting effective area estimates and the difference from the simulated effective area as an estimate for the uncertainty in the LAT effective area as a function of incident photon energy. This varies from <10% near 1 GeV to as much as 20% for energies below 0.1 GeV and 30% for energies greater than 10 GeV. Fluxes and errors are given in Table 2.

The gtlike fit for $0.1 < E < 30$ GeV is unbinned and results in a spectrum of the form

$$\frac{dN}{dE} = (2.08 \pm 0.04 \pm 0.13) \times 10^{-6} E^{\Gamma} e^{-E/E_c} \gamma \text{ cm}^{-2} \text{ s}^{-1} \text{ GeV}^{-1}, \quad (1)$$

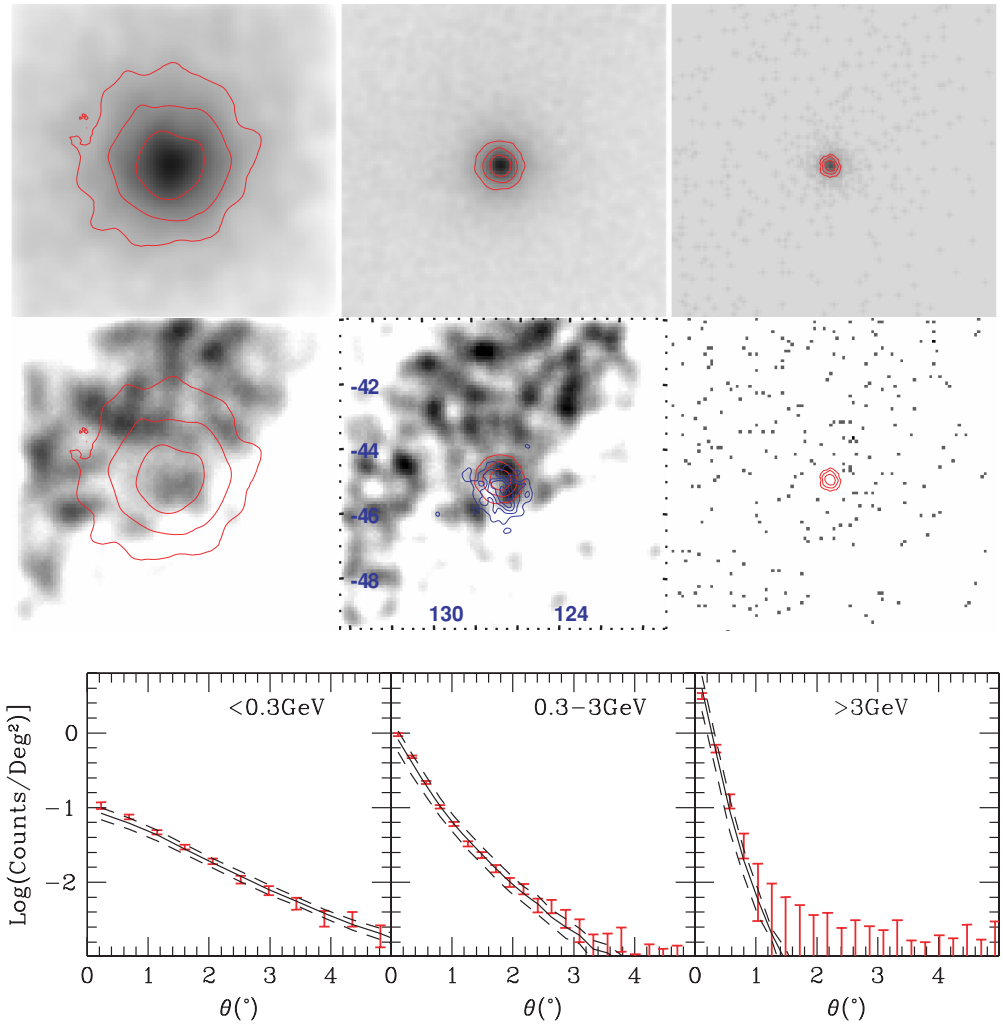

Figure 4. On- ($\phi = 0.05$–0.65, top row) and off- ($\phi = 0.65$–1.05, middle row) pulse phase images in three energy bands. Each panel spans $10^\circ \times 10^\circ$ in equatorial coordinates centered on Vela (R.A. and decl. marked in degrees in the central panel). On-pulse data are dominated by the point source; the panels have a hard square root stretch to show the faint wings of the PSF. The off-pulse images (linear grayscale) are dominated by Galactic diffuse emission; some of the structure is due to limited count statistics. Contours of the point source at 0.5, 0.25, and 0.125 of the peak intensity are shown (red) in each frame. In the middle energy off-pulse image, we also show the HESS Vela PWN contours (Aharonian et al. 2006; blue). Along the bottom row, background-subtracted Vela PSFs (red error bars give the statistical error in the observed counts) are compared with simulations based on prelaunch descriptions of expected LAT performance (solid lines) and estimates of the systematic uncertainty in the model PSF (dashed lines).

with E in GeV, $\Gamma = -1.51 \pm 0.01 \pm 0.07$ and $E_c = 2.857 \pm 0.089 \pm 0.17$ GeV. The first errors are the statistical values for the fit parameters, while the second errors are our propagated systematic uncertainties. The latter are particularly large for our spectral index parameter Γ because of the large uncertainty at present in the effective area at high and low energies. To explore the stability of this result, we also fit using three other spectral estimators. We used a standard XSPEC analysis with our best model response matrices, a binned maximum likelihood estimator which computes the on-pulse photon counts in a point source weighted aperture in excess of off-pulse background counts ('ptlike'), and a method which propagates the model spectrum through simulated instrument response to compare with observed pulsed source counts. For additional tests of the stability of the spectral fits, the data were also analyzed separately for "pointed" and "survey" observations, as well as for events in the front (thin radiator foil) and back (thick radiator foil) sections of the LAT detector. The fit parameters for the various data sets and analysis techniques, do have some statistically significant variation, but all were well within our presently estimated systematic errors, as listed in Equation (1). We believe that as our understanding of the LAT performance improves we should be able to substantially decrease these systematic uncertainties.

Figure 5 presents the spectral power $E^2 \frac{dN}{dE}$ along with this best-fit model. The binned spectral points are drawn from the ptlike analysis and show both the statistical error flags (bars with caps) and the inferred systematic error flags (bars without caps); the systematic errors dominate for all energies below 7 GeV. We also plot the EGRET data points of Kanbach et al. (1994). These lie well above the LAT points at high energy. Some studies (Baughman 2007; Stecker et al. 2008) suggest that the EGRET flux may have been overestimated at high energy, due to an underestimate of the EGRET background. Correcting for such an overestimate would bring the EGRET points into closer agreement with the LAT points.

We have also attempted to fit the data with a generalized cutoff model of the form $\mathrm{Exp}[-(E/E_c)^b]$. We find $b = 0.88 \pm 0.04^{+0.24}_{-0.52}$ so that models with a hyper-exponential behavior are well excluded. Taking into account the systematic errors, the

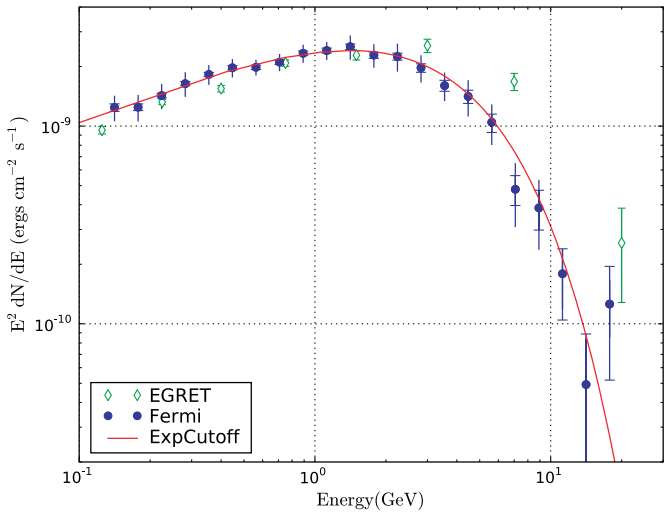

Figure 5. Phase-averaged Vela SED ($E^2 dN_\gamma/dE$). Both statistical (capped) and systematic (uncapped) errors are shown. We believe that the latter are conservative; they dominate at all energies below 7 GeV. EGRET data points (diamonds; Kanbach et al. 1994) are shown for comparison. The curve is the best-fit power law with a simple exponential cutoff.

(A color version of this figure is available in the online journal.)

spectrum is fully consistent with the simple exponential $b = 1$ cutoff. To check the exclusion of a given hyper-exponential model, we compute the probability of incorrect rejection of a given b value using the likelihood ratio test. For example, if only statistical errors are included $b = 2$ is rejected at 16.5σ; inflating the errors to the level of our estimated systematic uncertainty leads to a small, but not negligible, 0.29% chance of incorrectly rejecting the $b = 2$ model.

The analyses of Kanbach et al. (1980), Grenier et al. (1988), and Fierro (1995) already showed that there is significant spectral variation through the pulse, with the bridge region harder than the peaks. Clearly, in Figure 2 we see that the situation is even more complicated, with three or more overlapping physical components contributing to the energy-dependent pulse profiles. Also, in Figure 5, one sees that there may be emission in the highest energy bins in excess of a simple exponentially cutoff model. This likely arises from the extended hard spectrum of the P2 component and drives the best-fit value for b below 1. Clearly the phase-averaged spectrum is a superposition of emission from a variety of distinct physical regions, and we cannot expect a simple cutoff power-law spectral model to be an exact representation of the data. Reduced systematic errors and the photons of a year or more of LAT data will be required to explore the phase-resolved spectral structure.

5. DISCUSSION

5.1. Light Curve

The early LAT data have already greatly clarified the γ-ray emission of the Vela pulsar and, even before detailed phase-resolved spectral measurements and model comparisons, significantly constrain the origin of high-energy pulsar emission. Pulsar particle acceleration is believed to occur in the open zone, on the field lines above each magnetic pole which extend through the light cylinder. These subtend ~0.5 of pulsar phase at high altitude, so with a total phase in the narrow pulses of ~0.06 one would expect a comparable fraction of the open zone, and hence fraction of the spin-down power, to contribute to the γ-ray emission. The narrow peaks are often interpreted as caustics (Morini 1983; Romani & Yadigaroglu 1995; Dyks et al. 2004), where the combination of field retardation, aberration, and time delay causes emission from the boundary of an acceleration zone (gap) to pile up in pulsar phase. A simple pulse from a one-dimensional fold caustic would increase to a maximum as $I(\phi) \propto (\phi - \phi_0)^{-1/2}\theta[\phi - \phi_0]$ as one approaches the destruction of an image pair at phase ϕ_0 or fall off in mirror form after image pair creation. Vela's P2 structure with a slow rise and abrupt fall looks like a trailing (image pair destruction) caustic, albeit with a steeper increase to the maximum, suggesting intensity variation along the emission surface or a higher-order catastrophe. The shape of P1 is less clear, but the apparent fast rise and slow fall would indicate a leading (image pair creation) caustic (Figure 1).

The broad structure of the P3 interpulse region suggests a beam of emission from a bundle of field lines bracketed by the two caustic-forming zones. The similarity between the γ-ray P3 phase structure and that of the lower frequency optical/UV emission at $\phi \approx 0.25$ suggests a common origin—they both cover similar phase intervals and the peak shifts to later phase at higher energy. One appealing possibility is to associate the optical/UV P3 with synchrotron emission from relatively low-altitude pair cascades produced by the few-GeV curvature radiation dominating the νF_ν spectral energy distribution (SED). These $\gamma\gamma \longrightarrow e^\pm$ pairs, with electron energy $\gamma_e \sim 2\,\mathrm{GeV}/m_e c^2 \sim 10^{3.5}$, will produce synchrotron emission with characteristic peak energy $\epsilon \sim 12 B_{12}\gamma_e \sin\Psi_{-1}$ keV as they radiate away their pitch angle $\sim 0.1\Psi_{-1}$ radians in a magnetic field of 10^{12} G. For Vela, we have $B_{12} \sim 3(r/R_*)^{-3}$, so to produce $\epsilon \sim 5$ eV photons the pairs would reside at $r \sim 80\Psi_{-1}^{-1/3} R_*$, where R_* is the neutron star radius. If the synchrotron emission is outward beamed, along with the pairs, then the Compton-scattered flux would appear at $\sim\Psi\gamma_e^2\epsilon \sim 5$ GeV, matching the LAT P3 component. This suggests that the pulse of seed photons at IR to UV energies should have energy-dependent phase shifts tracking their Compton-up-scattered P3 progeny.

5.2. Luminosity and Beaming

While the VLBI parallax provides a well-determined distance of $D = 287^{+19}_{-17}$ pc, the pattern of the γ-ray beam and hence the true γ-ray luminosity are uncertain. To compute the true luminosity

$$L_\gamma = 4\pi f_\Omega F_{\mathrm{E,obs}} D^2 \tag{2}$$

we need a correction factor f_Ω from the observed phase-averaged energy flux $F_{\mathrm{E,obs}}$ at the Earth line of sight (at angle ζ_E to the rotation axis) to an average over the sky. For a given model, the correction depends on the geometry, so we have

$$f_\Omega(\alpha, \zeta_\mathrm{E}) = \int F_\gamma(\alpha, \zeta, \phi)\mathrm{d}\Omega/(F_{\mathrm{exp}} 4\pi), \tag{3}$$

where the model for a given magnetic inclination α from the rotation axis gives $F_\gamma(\alpha, \zeta, \phi)$, the pulse profile as a function of phase ϕ seen at viewing angle ζ. F_{exp} is the expected phase-averaged flux for the actual Earth line-of-sight ζ_E. In general highly aligned models, such as the polar cap scenario, have small sky coverage and $f_\Omega < 0.1$, while outer-magnetosphere models have much larger f_Ω (Romani & Yadigaroglu 1995). For Vela, the viewing angle is estimated to be $\zeta \approx 63^\circ$ from the geometry of the *Chandra X-Ray Observatory*-measured X-ray torus (Ng

& Romani 2008). The magnetic impact angle $\beta = \zeta - \alpha$ is constrained by the radio polarization data. Together, these allow us to compute the high-energy beam shape (assuming uniform emissivity along gap surfaces). For the outer gap (OG) picture, we compute $f_\Omega = 1.0$ for $\zeta = 64^\circ$. For the two-pole caustic (TPC) model appropriate to the slot-gap picture, we find $f_\Omega = 1.1$ (Watters et al. 2009).

The observed energy flux obtained by integrating E_γ times the photon number flux in Equation (1) over the range 0.1−10 GeV is $(7.87 \pm 0.33 \pm 1.57) \times 10^{-9}$ erg cm^{-2} s^{-1}. For a distance of 0.287 kpc, the γ-ray luminosity of Vela is then $7.8\times\ 10^{34} f_\Omega$ erg s^{-1}. Thus, the observed γ-ray flux implies an efficiency of $\eta_\gamma = 0.011 f_\Omega / I_{45}$ with $f_\Omega \geqslant 1$ for both the OG and TPC models. Note that this is a substantial fraction of the geometrical bound on the efficiency from the peak widths noted above.

5.3. Gamma-Ray Pulsar Models

Three general classes of models have been discussed for γ-ray pulsars. In polar cap models (Daugherty & Harding 1994, 1996; Sturner & Dermer 1995; Muslimov & Harding 2004), the particle acceleration and γ-ray production takes place in the open field line region within one stellar radius of the magnetic pole of the neutron star. In outer-gap (OG) models (Cheng et al. 1986; Romani 1996; Hirotani 2005), the interaction region lies in the outer magnetosphere in vacuum gaps associated with the last open field line. Other recent models hark back to the "slot-gap" picture of Arons (1983), with the polar cap rim acceleration extending to many stellar radii (Muslimov & Harding 2004).

The appreciable offset from the radio peak, coupled with the presence of only one radio pulse, suggests that the γ-rays arise at high altitude. This is also supported by the lack of hyper-exponential absorption in the spectrum, which is a signature of γ–B pair attenuation of low-altitude emission. The remaining two geometrical models can produce the general double peak profile of Vela (and many other γ-ray pulsars). In "OG" models, emission starts near the "null charge" $\Omega \cdot B = 0$ surface at radius $r_{\rm NC}$ and extends toward the light cylinder $r_{\rm LC} = cP/2\pi$. One magnetic pole dominates the emission in each hemisphere and the two peaks represent leading and trailing edges of the hollow cone of emission from this pole. If, on the other hand, emission extends well below the null charge surface toward the neutron star, both magnetic poles can contribute toward emission in a given hemisphere. This is the TPC model of Dyks & Rudak (2003) which might be realized in "slot-gap" acceleration models. In this case, the leading "image pair creation" caustic from high altitudes should not be visible, and the first γ-ray pulse represents the trailing caustic from emission at $r < r_{\rm NC}$ below the null-charge surface (the radio magnetic pole) while the second pulse represents a trailing caustic at higher altitudes from the opposite pole; both pulses should generally show a slow rise and steeper fall. Detailed γ-ray pulse profiles and, especially, phase-resolved spectra can help distinguish these scenarios.

Another geometric difference in the two scenarios is the origin of the emission outside the main pulse. Low-altitude field lines in the two-pole model tend to produce emission along all lines of sight. In the OG picture high-altitude field lines can contribute faint emission extending through the off-pulse region.

Further, as noted above, the energy spectrum also presents challenges for near-surface emission. In the polar cap models, a sharp turnover is expected in the few to 10 GeV energy range due to attenuation of the γ-ray flux in the magnetic field (Daugherty & Harding 1996). The spectral change at ∼2.9 GeV does not appear to fit this model. We conclude that low-altitude radiation subject to γ–B pair production cannot account for the bulk of the Vela γ-ray emission. Indeed, we can use the observed cutoff to estimate a minimum emission height as $r \approx (\epsilon_{\rm max} B_{12}/1.76\,{\rm GeV})^{2/7} P^{-1/7} R_*$, where $\epsilon_{\rm max}$ is the unabsorbed photon energy, P is the spin period, and the surface field is $10^{12} B_{12}$ G (Baring 2004). Using Vela parameters ($P = 0.089$ s, $B_{12} = 3.4$) we see that our cutoff implies that the bulk of the emission arises from $>2.2R_*$. Since we see pulsed photons up to $\epsilon_{\rm max} = 17$ GeV, this emission must arise at $r > 3.8R_*$. A similar conclusion has been recently made for the Crab pulsar by the MAGIC team, who observe pulsed $E > 25$ GeV emission, using the imaging air Cerenkov technique (Aliu et al. 2008). Finally, it should be noted that while typical radio pulsar emission is inferred to arise at relatively low altitudes, for Vela-type pulsars recent radio models infer emission heights of as much as $100R_*$ (Karastergiou & Johnston 2007). All of these factors point to a high-altitude origin of the Vela γ-ray emission.

6. SUMMARY

The early LAT observations of Vela serve to show that the instrument is performing very well, with effective area comparable to expectations, good PSFs, and excellent source localization, especially at high energies. The time tagging of events is excellent and our pulse profile reconstruction is limited primarily by the accuracy of the radio-derived pulsar ephemeris. This presently has an accuracy of ∼100 μs over our analyzed data span. The energy response and effective area calibration are currently being validated, but are at present known to ∼5% near 1 GeV, with uncertainties increasing to ∼20% at ⩽0.1 GeV and ∼30% at ⩾10 GeV.

These data also substantially improve our knowledge of the pulse properties of the Vela pulsar (PSR B0833-45) and are now placing important constraints on theoretical models. Already in these data we see that

1. The pulse profile is complex, with P1 and P2 dominated by very narrow components and substantial structure in the "bridge" region.
2. Although the P1 and P2 phases are very stable across the γ-ray band, the P1/P2 ratio decreases with energy. There is a distinct third peak in the "bridge" component which sharpens and moves to later pulsar phase with increasing energy.
3. While faint emission appears within ∼1° of the pulsar in the off-pulse phase, association if any with Vela is still unclear, due to the bright Galactic background in the vicinity. We thus quote an upper limit on the unpulsed point source flux, at 2.8% of the phase-averaged pulsed flux. A true PWN association will require additional data, allowing resolution at higher energies and a match to the radio and TeV images.
4. The phase-averaged γ-ray energy spectrum can be represented by a power law, with a exponential cutoff at 2.9 ± 0.1 GeV. The hyper-exponential cutoff index $b = 0.88 \pm 0.04^{+0.24}_{-0.52}$ is not significantly different from the simple exponential value $b = 1$. Large values of b, as expected for models radiating from the near-surface polar cap zone, are excluded.

During the first-year sky survey, we expect to collect approximately 1.3×10^5 additional pulsed Vela photons. This will allow a substantial increase in sensitivity to narrow pulse components.

We also expect improvements in our understanding of the instrument that will allow us to significantly reduce systematic errors. These two improvements will allow derivation of high-accuracy spectral properties in more than 100 bins of pulsar phase. These are the observational results that should let us pin down the location and energy distribution of the radiating particles. In turn, this should help us "reverse-engineer" this γ-ray machine and should provide substantial insight into the physics of pulsar magnetospheres.

The *Fermi* LAT Collaboration acknowledges the generous support of a number of agencies and institutes that have supported the development of the LAT. These include the National Aeronautics and Space Administration and the Department of Energy in the United States, the Commissariat à l'Energie Atomique and the Centre National de la Recherche Scientifique/Institut National de Physique Nucléaire et de Physique des Particules in France, the Agenzia Spaziale Italiana, the Istituto Nazionale di Fisica Nucleare, and the Istituto Nazionale di Astrofisica in Italy, the Ministry of Education, Culture, Sports, Science and Technology (MEXT), High Energy Accelerator Research Organization (KEK) and Japan Aerospace Exploration Agency (JAXA) in Japan, and the K. A. Wallenberg Foundation and the Swedish National Space Board in Sweden. The Australia Telescope is funded by the Commonwealth of Australia for operation as a National Facility managed by the CSIRO.

REFERENCES

Aharonian, F., et al. 2006, A&A, 448, L43
Aliu, E., et al. 2008, Science, 322, 1212
Arons, J. 1983, ApJ, 266, 215
Atwood, W. B., et al. 2009, ApJ, in press
Baring, M. G. 2004, Adv. Space Res., 33, 552
Baughman, B. 2007, PhD thesis, USCS
Caraveo, P., et al. 2001, ApJ, 561, 487
Cheng, K. S., Ho, C., & Ruderman, M. 1986, ApJ, 300, 522
Daugherty, J. K., & Harding, A. K. 1994, ApJ, 429, 325
Daugherty, J. K., & Harding, A. K. 1996, A&AS, 120, 107
Dodson, R., et al. 2003, ApJ, 596, 1137
Dyks, J., & Rudak, B. 2003, ApJ, 598, 1201
Dyks, J., et al. 2004, ApJ, 607, 939
Edwards, R. T., et al. 2006, MNRAS, 372, 1549
Fierro, J. M. 1995, PhD thesis, Stanford Univ.
Fierro, J. M., et al. 1998, ApJ, 494, 734
Frail, D. A., et al. 1997, ApJ, 475, 224
Grenier, I. A., Hermsen, W., & Clear, J. 1988, A&A, 204, 117
Harding, A. K., et al. 2002, ApJ, 576, 376
Helfand, D. J., Gotthelf, E. V., & Halpern, J. P. 2001, ApJ, 556, 380
Hirotani, K. 2005, Ap&SS, 297, 81
Hobbs, G. B., Edwards, R. T., & Manchester, R. N. 2006, MNRAS, 369, 655
Kanbach, G., et al. 1980, A&A, 90, 163
Kanbach, G., et al. 1994, A&A, 289, 855
Karastergiou, A., & Johnston, S. 2007, MNRAS, 380, 1678
Large, M. I., Vaughan, A. E., & Mills, B. Y. 1968, Nature, 220, 340
Manzali, A., De Luca, A., & Caraveo, P. A. 2007, ApJ, 669, 570
Morini, M. 1983, MNRAS, 202, 495
Muslimov, A. G., & Harding, A. K. 2004, ApJ, 606, 1143
Ng, C.-Y., & Romani, R. W. 2008, ApJ, 673, 411
Pavlov, G. G., et al. 2003, ApJ, 591, 1157
Pellizzoni, A., et al., 2009, ApJ, 695, L115
Romani, R. W. 1996, ApJ, 470, 469
Romani, R. W., Kargaltsev, O., & Pavlov, G. G. 2005, ApJ, 627, 383
Romani, R. W., & Yadigaroglu, I.-A. 1995, ApJ, 438, 314
Smith, D. A., et al. 2009, A&A, 492, 923
Stecker, F. W., Hunter, S. D., & Kniffen, D. A. 2008, Astropart. Phys., 29, 25
Sturner, S. J., & Dermer, C. D. 1995, Adv. Space Res., 15, 77
Thompson, D. J. 2001, in AIP Conf. Proc. 558, High Energy Gamma Ray Astronomy, ed. F. A. Aharonian & H. J. Volk (Melville, NY: AIP), 103
Thompson, D. J., et al. 1975, ApJ, 200, 79L
Watters, K., et al. 2009, ApJ, 695, 1289